ISBN: 978-3-95450-191-5 doi:10.18429/JACoW-SRF2017-THPB026

INVESTIGATION OF THE EFFECT OF STRATEGICALLY SELECTED GRAIN BOUNDARIES ON SUPERCONDUCTING PROPERTIES OF SRF CAVITY NIOBIUM*

M. Wang, T.R. Bieler, Michigan State University, East Lansing, MI 48824, USA
C.C. Compton, Facility for Rare Isotope Beams, East Lansing, MI 48824, USA
S. Balachandran, S. Chetri, A. A. Polyanskii, P. J. Lee, Applied Superconductivity Center, National High Magnetic Field Laboratory, Tallahassee, FL 32310, USA

Abstract

High purity Nb is commonly used for fabricating SRF cavities due to its high critical temperature and good formability. However, microstructural defects such as dislocations and grain boundaries in niobium can serve as favorable sites for pinning centers of magnetic flux that can degrade SRF cavity performance. In this study, six bi-crystal niobium samples extracted from strategically selected grain boundaries from two niobium disks were investigated for the effect of grain misorientation on magnetic flux behavior. Laue X-ray and EBSD-OIM crystallographic analysis were used to characterize grain orientations and orientation gradients. Cryogenic Magneto-Optical Imaging (MOI) was used to directly observe magnetic flux penetration at about 5-8 K. Flux penetration was observed along one of the grain boundaries, as well as along a low angle boundary that was not detected prior to MOI imaging. Hydride scars on the sample surface after MOI were examined using Atomic Force Microscopy (AFM) analysis. The relationships between dislocation content, cryo-cooling, flux penetration, and grain boundaries are examined.

INTRODUCTION

Superconducting radio-frequency (SRF) cavities, which have been used for charged particle accelerators for decades, are usually made from high purity niobium because of its highest critical temperature and magnetic field of elemental superconductors, as well as its good formability, reliable chemical stability, and sufficient availability on the market [1].

Achieving a high accelerating field and quality factor has always been the major motivations for the research and development of niobium cavities. Over the past decades, the theoretical limit of accelerating field for niobium has been achieved at about 42MV/m [2-4], however the high performance of SRF cavities cannot always be consistently reproduced due to the variability of the material.

Microstructural defects such as grain boundaries and dislocations, which are introduced during the fabrication and processing of niobium cavities, are capable of trapping magnetic flux, which would result in the loss of superconductivity in local regions and cause perturbation to the superconducting current in niobium [5-9]. Grain boundaries play a critical role in defining niobium cavity performance, since they are both a source and a sink for microstructural defects. During recrystallization, grain boundaries sweep across the grain and eliminate dislocations in their way, and hydrogen atoms and vacancies tend to be stored in grain boundaries, favoring precipitation of hydrides. Although magnetic flux trapped by grain boundaries and dislocations in niobium cavities is widely acknowledged as a common reason for RF losses, the mechanism is still not clear.

To pursue reproducible cavity performance, it is necessary to comprehensively understand the mechanism of flux trapping by grain boundaries of different types. This paper focuses on grain boundaries that were strategically chosen such that specific slip system, at different angles with respect to the grain boundaries, will be activated when tensile strain is imposed that favors shear along the boundary. Two bi-crystal samples were extracted with favored slip systems parallel to the grain boundaries, while four other samples have slip systems perpendicular to the grain boundaries. The purpose is to introduce dislocations under various orientations of grain boundaries of different types. Cryogenic Magneto-Optical Imaging (MOI) was used to directly observe magnetic flux behavior and the orientation gradient, and low angle grain boundary were characterized using Electron Backscattered Diffraction (EBSD) and Orientation Imaging Microscopy (OIM) crystallographic analysis. Only two undeformed samples will be described in this paper, which provides the basis for comparison that will be reported in future work.

MATERIALS AND SAMPLE EXTRACTION

Large Grain Niobium Disks

A niobium disk, with a thickness of 2.8 mm and a diameter of 270 mm, was sliced from a high purity large grain niobium ingot. It consists of several large grains with visible grain boundaries (Fig. 1a), which enables bi-crystal sample design along different boundaries. Prior tensile sample characterization is found in ref. [2].

Laue X-ray Diffraction and Grain Orientations

To obtain information of crystal orientations of those numbered grains in the niobium disk, Laue X-ray diffraction patterns of these grains were collected, which were then indexed using the OrientExpress software to

* Research supported by DOE/OHEP contracts DE-SC0009962, DE-SC0009960, NSF-DMR-1157490, and the State of Florida.

ISBN: 978-3-95450-191-5 doi:10.18429/JACoW-SRF2017-THPB026

generate Bunge Euler angles of the selected grains, as shown in Table 1. These Bunge Euler angles represent the orientations that can be used to plot the sample normal direction orientation map shown in Fig. 1b. Grains 6, 9, and 10 were selected to extract bi-crystal samples.

Table 1: Bunge Euler angles (in degrees) of Numbered Grains Measured Using Laue X-ray Diffraction

Grain #	φ_1	Φ	φ_2
6	186	37	173
9	271	159	185
10	245	140	154

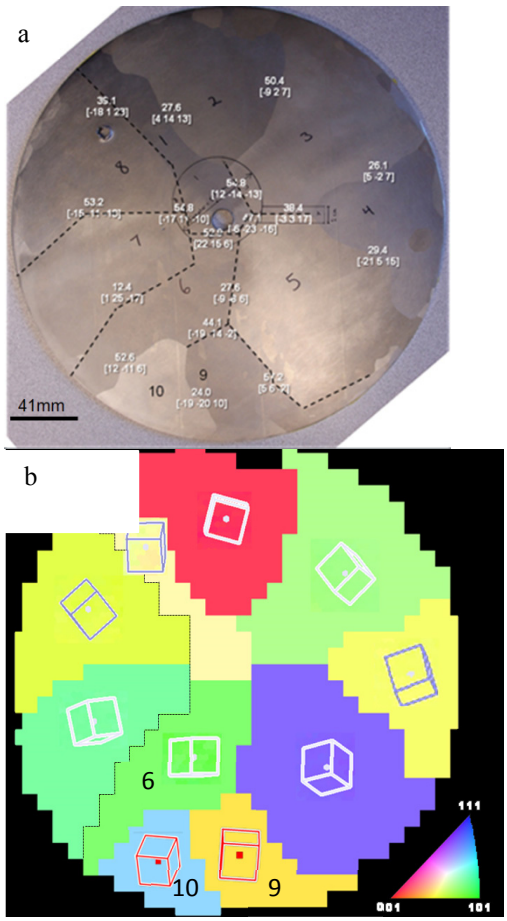

Figure 1: (a) A niobium disk with visible grain boundaries sliced from a large-grain ingot. (b) Normal direction orientation map, where grains are colored by the crystal directions that are parallel to the disk normal.

Schmid Factor Calculation and Bi-crystal Design

When stress is applied to the material, the likelihood of the activation of a slip system can be described by Schmid factor, which ranges from 0 to 0.5 with 0.5 indicating the orientation with the highest possible resolved shear stress on a given slip system. Therefore, the Schmid factor calculation identifies the operational slip systems and enables design of bi-crystals with orientations that favor specific slip systems.

A MATLAB code was developed to calculate the Schmid factors for all 48 slip systems of BCC crystals over a 360° rotation around the Z axis (disk normal direction). Figure 2a shows the plot of the Schmid factor of (321) $[\bar{1}11]$ slip system in Grain 6, which is approximately parallel to the grain boundary between Grain 6 and Grain 10. About 10° rotation is needed to reach the desired orientation that makes (321) $[\bar{1}11]$ slip system the most favored. Figure 2b shows the four most favored slip systems, represented by cubes, with $[\bar{1}11]$ direction after the 10° rotation. The shaded planes and turquoise lines represent slip planes and Burgers vector directions respectively. The tensile axis can be chosen according to this plot to make (321) $[\bar{1}11]$the most favored slip system (also see Fig. 3a).

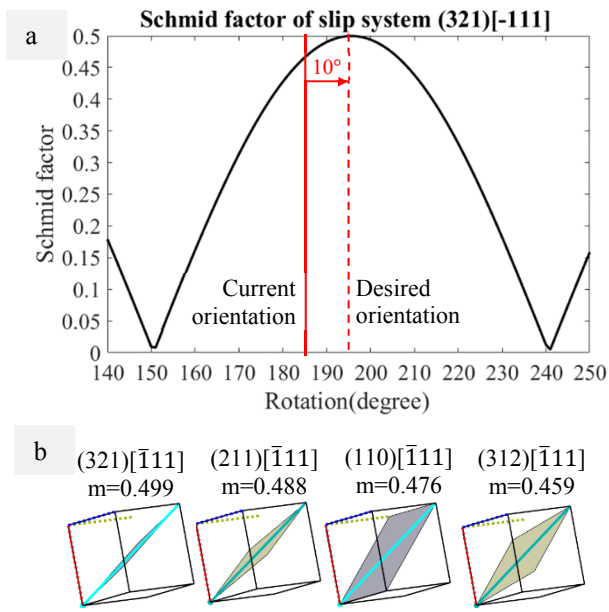

Figure 2: (a) Schmid factor calculation based on the orientation of Grain 6 (for the rotation range between 140° and 250°). The red solid line marks the reference orientation and the red dashed line marks the desired orientation with the highest Schmid factor. (b) Slip systems and crystal orientation after a 10° rotation represented by cubes with dislocation Burgers vectors (turquoise lines), slip planes (shaded planes), and Schmid factors (m values) noted.

The sample design strategy was to make bi-crystal samples with a slip system that is highly favored in one of the two grains and nearly parallel to the grain boundary. Two bi-crystal tensile samples and one bi-crystal cylindrical sample were extracted from each of the two chosen grain boundaries as shown in Fig 3a. The slip systems that are parallel to the grain boundaries in Grains 6 and 9 are chosen such that they are the most favored when the tensile axis is set at the angle indicated. Figures 3b and 3c show the overlaid images of top and bottom of the extracted cylindrical bi-crystal samples. Sample

ISBN: 978-3-95450-191-5 doi:10.18429/JACoW-SRF2017-THPB026

GB6-10 extracted from Grains 6 and 10 has a grain boundary with a misorientation of 53° and is tilted from the surface by 14°, while Sample GB10-9 extracted from the Grain 10-9 boundary has a boundary perpendicular to the disk surface with a misorientation of 24°. The tensile specimens will be discussed in a future paper. The un-deformed cylindrical samples between the tensile samples are examined further using MOI and EBSD-OIM.

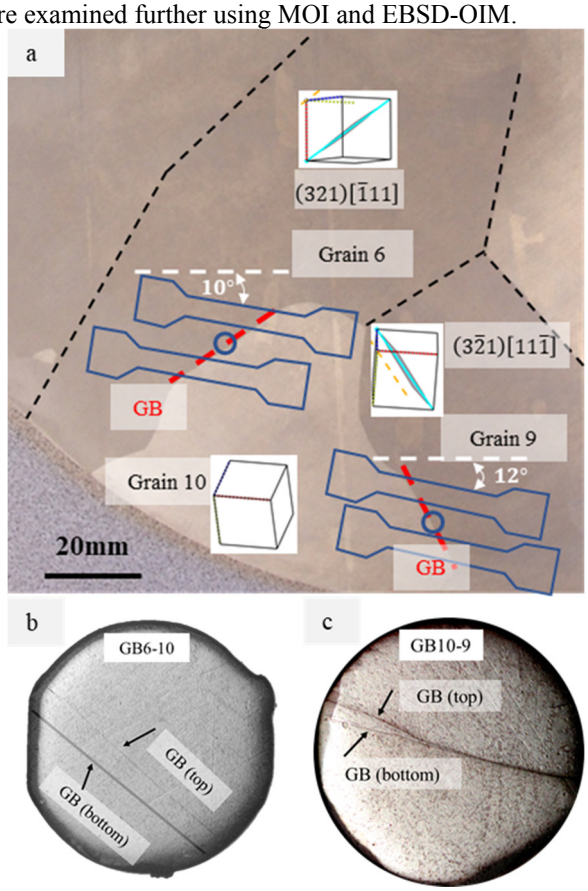

Figure 3: (a): Layout of bi-crystal samples extracted from the niobium disk with grain orientations and slip systems represented by prisms, which need to be rotated by the angle indicated to reach the most favored orientations. (b) and (c): Overlaid images of top and bottom of Sample GB6-10 showing a 14° tilted boundary, and GB10-9 showing a grain boundary perpendicular to the surface.

RESULTS

Magnetic Flux Penetration

The MOI technique enables the possibility of visualizing both local and global magnetic flux behavior, and hence the effect of microstructural defects in niobium on magnetic flux penetration below the critical temperature ($T_C = 9.3K$) [5, 10]. After vibrational polishing and buffered chemical polishing both GB6-10 and GB10-9 were characterized using MOI with the magnetic field applied perpendicular to the sample surface and the Magneto-Optical (MO) images are shown in Fig. 4, where the bright contrast indicates the existence of magnetic flux.

The grain boundaries are visible on the polished sample surfaces as shown in Figs. 4a and 4d. In GB10-9, a magnetic field over 50 mT caused preferential magnetic flux penetration from both ends of the grain boundary. Also, preferential flux penetration is evident along a curved path without visible boundaries, which is the location of a Low Angle Grain Boundary (LAGB) (next section). The full length of the grain boundary was penetrated with H=73.2mT. At the same temperature, MO images of Sample GB6-10 did not show any preferential flux penetration along the grain boundary. Rather, the whole circumference of the sample was penetrated with a much lower magnetic field of 16.4 mT.

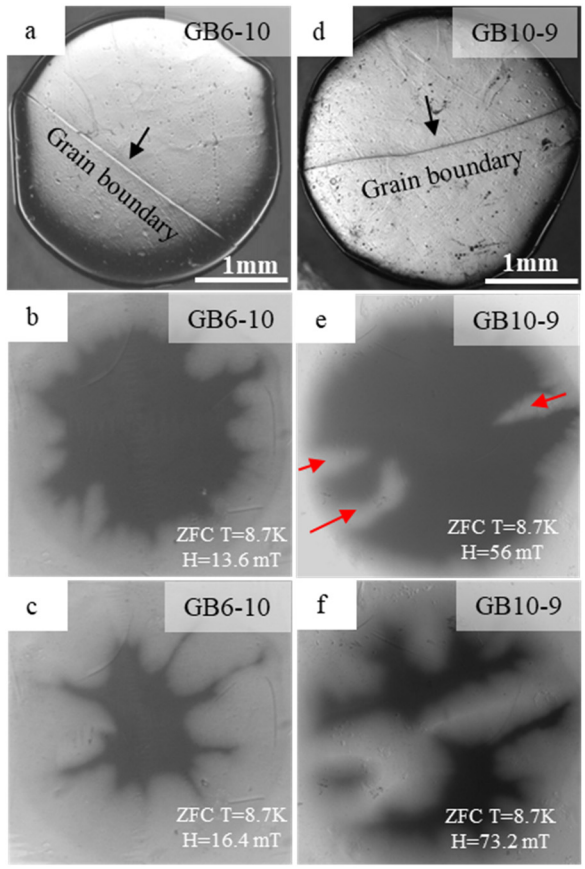

Figure 4: Optical and MO images of Sample GB6-10 (a, b, c) and Sample GB10-9 (d, e, f). MO images were taken in Zero-Field-Cooled (ZFC) condition with temperature T and magnetic field H indicated in the figure.

OIM-EBSD Characterization

To explore the reasons for the curved preferential magnetic flux penetration along a path without visible grain boundaries, SEM based EBSD-OIM analysis was done to determine if LAGB could account for the curved flux penetration.

LAGBs, with 2~3° misorientation, are clearly revealed in the IPF map (Fig. 5b) and lined up with the curved flux penetration shown in Figs. 4e and 4f. This proves that the curved flux penetration was caused by a LAGB that was

ISBN: 978-3-95450-191-5 doi:10.18429/JACoW-SRF2017-THPB026

not visible in optical images. Figure 5c shows an additional LAGB that branches off the more visible LAGB.

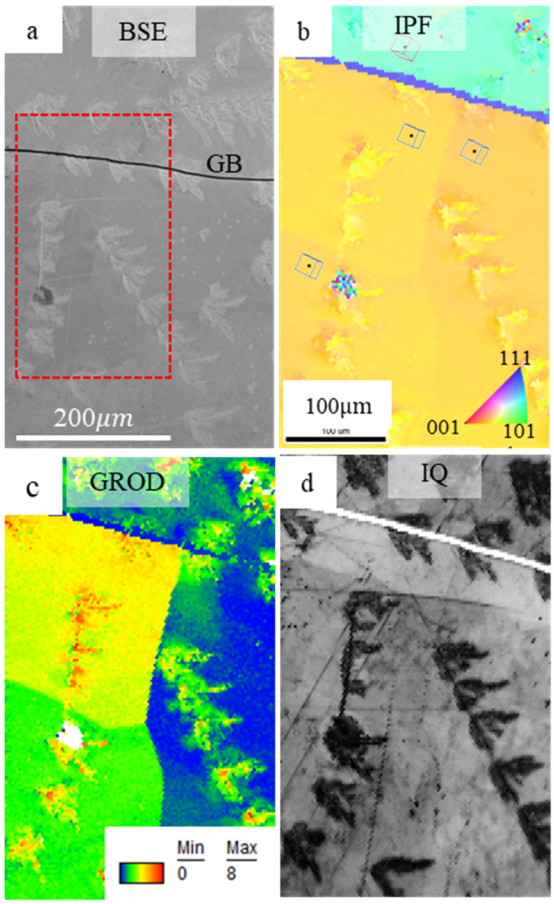

Figure 5: Maps from EBSD-OIM analysis of the sample surface after MOI. The Backscattered Electron (BSE) image was taken in the curved flux penetration area with a red dashed box indicating the EBSD scanned region, from which Inverse Pole Figure (IPF) (b), Grain Reference Orientation Deviation (GROD) (c), and Local Average Misorientation (LAM) maps (d) were generated.

After the MOI test, where the sample experienced a cryogenic cycle, the BSE image (Fig. 5a) of the sample surface shows many hydride scars, which result from the precipitation of niobium hydrides at the cryogenic temperature. These hydrides were then re-absorbed by the niobium matrix when the temperature went back to room temperature. The hydride scars are distributed inside the subgrains, instead of along the LAGBs, suggesting that they formed preferentially in residual deformation regions underlying surface scratches, which can be observed in the IQ map in Fig. 5d. This differs from the observation in ref [11], which reported hydrides forming along LAGBs.

An AFM scan was performed on a hydride scar to investigate the topography of the feature, as shown in Fig. 6. Hydride scars, usually arranged in rows, consist of a lower region surrounded by mountain-range-like higher areas, which are caused by a volume expansion from precipitation of hydrides that deformed the surrounding matrix niobium [12]. The height difference of the hydride scar area is around 0.3~0.4 μm. While these large hydride scars can be prevented with more strategic cooling schedules, they provide insight about the potential for generating dislocation debris. Clearly, these large scars did not cause flux penetration, but flux penetration did occur in the boundaries in which no hydride scars are visible.

AFM Maps of Niobium Hydride Scars

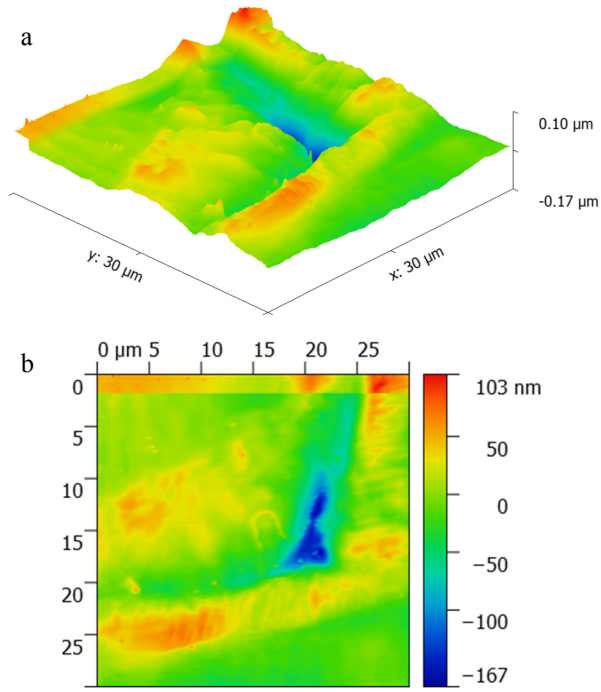

Figure 6: 2-D (a) and 3-D (b) AFM maps of a hydride scar on the sample surface after MOI.

DISCUSSION

The significant differences in the MOI results of the two GB6-10 and GB10-9 can be attributed to the lack of a perpendicular angle between the boundary and the sample surface in sample GB6-10 with a 53 °/[12, -11, 6] misorientation, while GB10-9, which showed premature flux penetration, has a boundary perpendicular to the sample surface and the misorientation is 24°/[-19, -20, 10]. This is consistent with a previous study, which compared the magnetic flux behavior in two niobium bi-crystals with different grain boundary orientations. Under an external field applied perpendicular to the sample surface, MO images of the bi-crystal with a perpendicular grain boundary with misorientation of 17° showed preferential flux penetration at T=6K, H=80mT, while the bi-crystal with a 35° tilted boundary with misorientation of 36°did not reveal any grain boundary flux penetration [5]. Flux penetration along a LAGB following 5% strain in single-crystal niobium was also observed in ref [11], which provides additional evidence for LAGB flux penetration. As there are abundant LAGBs in cryo-cooled SRF niobium even without any prior deformation, at least

ISBN: 978-3-95450-191-5 doi:10.18429/JACoW-SRF2017-THPB026

some LAGBs are weak spots that may degrade the cavity performance. Removal of LAGBs is only possible with migration of high angle boundaries, resulting from recrystallization or grain growth, which is not likely to occur uniformly in large grain material.

These two MOI characterized bi-crystals show that magnetic flux trapping does not occur on all boundaries, implying that additional features of grain boundaries such as tilting angles and misorientations are responsible for flux penetration.

Hydride scars were observed on the sample surface after cryogenic cooling and MOI, and the scar area, with a height difference roughly at 0.3~0.4 μm, could cause disturbance to the superconducting electrons, but they do not appear to cause flux penetration.

Future study of the effect of deformation of the bi-crystal tensile samples will provide further understanding of the relationship between flux trapping, dislocations, and grain boundaries of different types.

CONCLUSIONS

Flux penetration has been observed in both low- and high-angle boundaries, but these boundaries need to be perpendicular to the surface, for preferential flux penetration to occur. Uniform flux penetration at much lower fields was observed in a bicrystal sample with a grain boundary not parallel to the beam, with a higher misorientation angle. The results to date show that there is no clear indicator for flux penetration prediction, but the number of observations is still small. The fields at which flux trapping occur also depend on microstructural features, and needs to be more extensively compared and studied.

REFERENCES

[1] Singer, W., "SRF Cavity Fabrication and Materials," arXiv preprint arXiv:1501.07142, 2015.

[2] Bieler, T.R. *et al*., "Physical and mechanical metallurgy of high purity Nb for accelerator cavities," Physical Review Special Topics - Accelerators and Beams, 2010. **13**(3): p. 031002.

[3] Ciovati, G., "Effect of low-temperature baking on the radio-frequency properties of niobium superconducting cavities for particle accelerators," Journal of Applied Physics, 2004. **96**(3): p. 1591-1600.

[4] Saito, K. "State-of-the-Art and Future Prospects in RF Superconductivity," in Proceedings of IPAC2012, New Orleans, Louisiana, USA. 2012. p. 11-15.

[5] Polyanskii, A. *et al*., "Magneto-Optical Study High-Purity Niobium for Superconducting RF Application," in AIP Conference Proceedings-American Institute of Physics. 2011. p. 186-202.

[6] Asavari, S.D. *et al*., "Flux pinning characteristics in cylindrical niobium samples used for superconducting radio frequency cavity fabrication," Superconductor Science and Technology, 2012. **25**(6): p. 065014.

[7] Aull, S., O. Kugeler, and J. Knobloch, "Trapped magnetic flux in superconducting niobium samples," Physical Review Special Topics - Accelerators and Beams, 2012. **15**(6): p. 062001.

[8] Posen, S. *et al*., "Flux expulsion variation in SRF cavities," in 17th International Conference on RF Superconductivity. 2015. Whistler, BC, Canada: p. 404-408.

[9] Matsushita, T., "Flux pinning in superconductors," Vol. 164. 2007, New York: Springer.

[10] Polyanskii, A., D. Feldmann, and D. Larbalestier, "Magneto-optical characterization techniques," The Handbook on Superconducting Materials," Edited by David Cardwell and David Ginley, Institute of Physics UK, 2003. **1551**.

[11] Sung, Z.-H. *et al*., "Development of low angle grain boundaries in lightly deformed superconducting niobium and their influence on hydride distribution and flux perturbation," Journal of Applied Physics, 2017. **121**(19): p. 193903.

[12] Birnbaum, H., M. Grossbecr, and M. Amano, "*Hydride precipitation in Nb and some properties of NbH.* Journal of the Less Common Metals, 1976. **49**: p. 357-370.